

A Protection System for Inverter Interfaced Microgrids

Ehsan Dehghanpour[✉], Student Member, IEEE, Michel Normandeau, Member, IEEE,
Géza Joós[✉], Life Fellow, IEEE, and Yves Brissette, Life Senior Member, IEEE

Abstract—One of the main challenges in the protection of the Inverter-Based Microgrids (IBM) is fault detection. Inverter-based resources have limited fault current; they also adopt different control schemes which make their fault current analysis and estimation more complex. These features make the traditional protection schemes inapplicable in IBMs. In this paper, two parameters are introduced and a protection scheme is proposed based on the introduced parameters to protect feeders and Distributed Generators (DGs) in IBMs. In the proposed scheme, in each sampling window, the last samples of the current waveform are predicted and the difference between the actual samples and the predicted samples are obtained; the voltage phase angle shift between the present and the past sampling windows is also computed; using these parameters and by introducing a new relay characteristic based on Mahalanobis distance the fault is detected in IBM. The effectiveness of the proposed protection scheme is verified through the simulation and experiment results.

Index Terms—Power distribution protection, microgrid protection, inverter, fault detection.

I. INTRODUCTION

MICROGRID is defined as a group of interconnected loads and distributed energy resources with clearly defined electrical boundaries that act as a single controllable entity with respect to the grid and can connect and disconnect from the grid to enable it to operate in both grid-connected or island modes [1]. Microgrid is considered as an alternative to solve the energy crisis and decrease carbon dioxide emissions by utilizing distributed renewable energy resources. Inverters are employed as the interface between the microgrid and the energy sources, which leads to the formation of the inverter-based microgrid concept. Inverters are used to improve the controllability and power quality of distributed energy resources [2]–[3]. However,

Manuscript received March 22, 2021; revised June 11, 2021 and July 28, 2021; accepted August 28, 2021. Date of publication September 3, 2021; date of current version May 24, 2022. This work was supported in part by the Natural Sciences and Engineering Research Council of Canada/Hydro-Québec Industrial Research Chair on the Integration of Renewable Energies and Distributed Generation into the Electric Distribution Grid Paper no. TPWRD-00474-2021. (*Corresponding author: Ehsan Dehghanpour*)

Ehsan Dehghanpour and Géza Joós are with the Department of Electrical and Computer Engineering, McGill University, Montréal, QC H3A 0G4, Canada (e-mail: ehsan.dehghanpour@mail.mcgill.ca; geza.joos@mcgill.ca).

Michel Normandeau and Yves Brissette are with the Hydro-Québec Research Institute, Varennes, QC J3X 1S1, Canada (e-mail: normandeau.michel@hydroquebec.com; brissete6@hotmail.com).

Color versions of one or more figures in this article are available at <https://doi.org/10.1109/TPWRD.2021.3110199>.

Digital Object Identifier 10.1109/TPWRD.2021.3110199

inverter-based resources (IBRs) have raised many challenges when it comes to the fault detection and protection [4]–[5]. Inverters adopt different control schemes which make their fault current analysis and estimation more complex [6]–[7], and they may become disconnected from the microgrid in the first 3 to 7 AC cycles after a fault [8], [9]. Moreover, the fault current magnitude varies significantly when microgrid transfers from the grid-connected to the island mode of operation [4]–[5]. The fault current coming from the main grid is comparatively large in the grid-connected mode. In contrast, in the island mode of operation, the fault current is relatively small. Besides, the fault current contribution of IBRs is different from the traditional synchronous generators; this is because of the current control loop embedded in the inverter control system, which limits the maximum output current to 1.2 to 2 p.u [10]–[11]. Therefore, the main challenge in front of microgrid protection is the fault detection. The fault detection is an integral part of any protection scheme, and until now, many researches have been conducted on the fault detection in microgrids. In [12], a negative-sequence resistance-based fault detection approach to detect the fault in the islanded IBM is proposed but the method only detects faults in the island mode of operation. A fault detection and classification scheme for the microgrid based on the wavelet transform and deep neural network is presented in [13]; by using Hilbert–Huang transform and machine learning techniques, authors proposed a fault detection scheme for the microgrid in [14]; these methods use many branch currents and their performance are affected by missing data or the resolution of the training dataset. In [15], a fault detection method is introduced that detects the fault using positive sequence voltage and current; the authors in [16] proposed a modified classical fault detection technique that is working based on the negative sequence component, but these methods have not considered inverters’ unconventional response in the sequence domain. The method proposed in [17] uses fifth harmonic injection after fault occurrence to detect the fault in the islanded microgrid; to achieve this, an auxiliary control loop should be embedded in the inverter’s control system which is not always feasible; also, the method is only able to detect faults in the island mode. An adaptive fault detection method based on positive and negative superimposed currents is proposed in [18], but the characteristic of the sequence impedance in IBMs has not been considered. In [19] and [20] microgrid protection schemes based on the differential protection principle are presented. Because of its nonsusceptibility to bidirectional power flow, number of DGs in the microgrid, and weak infeed, the

differential protection principle may meet the requirements to protect the microgrid. However, differential protection relies on the high-bandwidth communication to detect the fault, which increases the implementation cost; besides, as the penetration of IBRs increases in the system, the traditional differential relays may become ineffective because of the difference between the sequence components of the fault currents on both sides of the line in the inverter-based systems [21], [22].

Although different methods are presented in the literature to detect the fault in the microgrids, the lack of a comprehensive protection scheme for IBM still exists. In other words, no presented IBM protection scheme includes all of the following features: (a) Detecting all types of faults; (b) Detecting the fault in less than 3 AC cycles after fault [9]; (c) Not to be relying on high-bandwidth communication to detect the fault; (d) Being independent from the inverter's control strategy; (e) Detecting the fault in both microgrid's operating modes.

In this paper, voltage Phase Angle Shift (PAS) and D parameters are introduced and a comprehensive protection scheme is presented. The method detects the fault by measuring the PAS and D parameters and employing a new relay characteristic based on Mahalanobis Distance (MD). The main causes of the PAS are the difference in the X/R ratio between the source and the faulted feeder, the transformation of sag to lower voltage levels, and active and reactive power variations which happen following a fault. Also, the D parameter is defined as the difference between the predicted and the actual current samples. The proposed scheme uses the local information to detect the fault; it detects all fault types including impedance faults in less than 1 AC cycle (16 milliseconds); it also detects the fault in both microgrid operation modes.

The rest of the paper is organized as follows: in Section II, the proposed protection scheme is introduced; the simulation results are presented in Section III; finally, experiment results and conclusion are presented in Sections IV and V, respectively.

II. PROPOSED PROTECTION SCHEME

In this paper, the voltage Phase Angle Shift (PAS) and D parameters are introduced and employed to detect the feeder faults in IBMs. These parameters and the proposed protection scheme are explained in the following subsections.

A. Voltage Phase Angle Shift (PAS)

A short circuit in the system not only causes a voltage magnitude drop but a change in the voltage phase angle as well. The main causes of the voltage phase angle shift are the difference in the X/R ratio between the source and the faulted feeder, the active and reactive power variation and their effects on frequency and voltage level, and the transformation of the sag to lower voltage levels. This phase angle shift is referred to as a phase angle shift associated with the voltage sag that demonstrates itself as a shift in the zero-crossing point of the instantaneous voltage [23]–[25].

Consider the voltage waveform and the sampling windows shown in Fig. 1. In this figure, the sampling frequency is 16 samples per cycle. The red window shows the present sampling

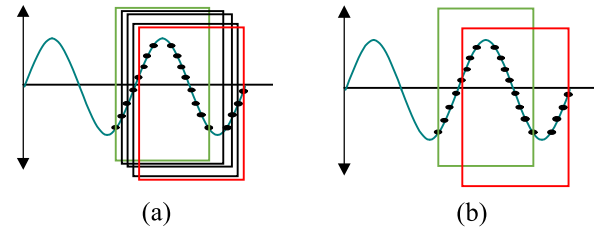


Fig. 1. (a) Moving sampling window. (b) Present and past sampling windows.

window, and the green window depicts the past sampling window which is placed 4 sampling windows behind the present sampling window. Both present and past sampling windows are shown in Fig. 1(b). In normal conditions, the phase difference between the sampling windows shown in Fig. 1(b) is $((360/16)*4 = 90$ degrees. In other words, if the past sampling window is shifted forward by 90 degrees, the two waveforms are exactly in phase. But when a fault occurs, the phase difference between the present and past sampling windows changes. If in the given example, the phase difference is either more or less than 90 degrees, this can be an indication of a fault.

1) *Voltage Phase Angle Shift Calculation:* In order to measure the phase angle shift, the fundamental component of the present and past sampling windows are obtained using the Least Squares (LS) approach. Consider the sampled voltage based on the Fourier series as shown in Eq. (1).

$$V(kT_s) = \sum_{n=1}^N A_n \sin(n\omega_0 kT_s) + B_n \cos(n\omega_0 kT_s) \quad (1)$$

Where N is the maximum harmonic order of the voltage; ω_0 is the fundamental angular frequency; T_s is the sampling period, and $V(kT_s)$ is the k th component of the voltage vector V:

$$\begin{aligned} V^T = & [V(t_0 + T_s) \ V(t_0 + 2T_s) \ V(t_0 + 3T_s) \\ & \dots \ V(t_0 + KT_s)] \end{aligned} \quad (2)$$

Vector V contains all measured voltage samples within one cycle, and K is the total number of samples in one cycle. Therefore, the vector form of Eq. (1) can be written as Eq. (3).

$$V = SY \quad (3)$$

where Y is the unknown coefficient matrix, and S is known signals. Since only the fundamental frequency needs to be estimated here, $Y^T = [A_1, B_1]$ and S can be considered as the following:

$$S^T = \begin{bmatrix} \sin(\omega_0 T_s) & \sin(\omega_0 2T_s) & \dots & \sin(\omega_0 KT_s) \\ \cos(\omega_0 T_s) & \cos(\omega_0 2T_s) & \dots & \cos(\omega_0 KT_s) \end{bmatrix} \quad (4)$$

Using LS approach, the fundamental frequency component of the voltage can be estimated as Eq. (5) and Eq. (6) demonstrate.

$$Y = (S^T S)^{-1} S^T V \quad (5)$$

$$\hat{V} = S (S^T S)^{-1} S^T V \quad (6)$$

where \hat{V} is the estimated fundamental component of the measured voltage. LS approach is employed here to estimate the

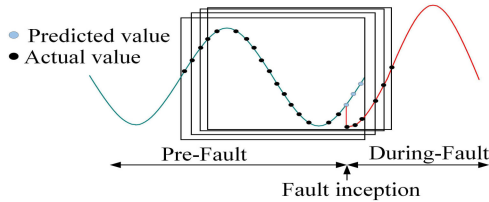


Fig. 2. Moving sampling window; predicted and actual samples.

fundamental frequency component of the signal fast; it should be mention that $S(S^T S)^{-1} S^T$ is a constant matrix and can be computed off-line and stored. When the fundamental components of the present and past sampling windows are calculated, the phase difference between the present and past sampling windows can be obtained by computing the scalar product of \hat{V}_{pr} and \hat{V}_{pa} that are the estimated fundamental component vector of the present sampling window and the estimated fundamental component vector of the past sampling window, respectively.

$$\hat{V}_{pr} \cdot \hat{V}_{pa} = |\hat{V}_{pr}| |\hat{V}_{pa}| \cos(\varphi) \quad (7)$$

$$\varphi = a \cos \left(\frac{\hat{V}_{pr} \cdot \hat{V}_{pa}}{|\hat{V}_{pr}| |\hat{V}_{pa}|} \right) \quad (8)$$

In the above equations, φ is the phase difference between the two vectors in radian; $|\hat{V}_{pr}|$ and $|\hat{V}_{pa}|$ are Euclidian length of \hat{V}_{pr} and \hat{V}_{pa} respectively.

Therefore, the net Phase Angle Shift (PAS) between the fundamental component of the present and past sampling windows is:

$$PAS = \left| \frac{\varphi \times 180}{\pi} - \frac{\alpha \times 360}{K} \right| \quad (9)$$

Where K is the number of samples in one cycle, and α is the number of samples between the present and past sampling windows. For example, in the given example in Fig. 1(b) $\alpha = 4$ and $K = 16$; therefore, in normal conditions PAS is 0, and if the PAS is greater than zero it can be an indication of the fault. α should be tuned by considering the sampling frequency and can be chosen between $0.1K$ to $0.25K$.

B. D Parameter: Difference Between Predicted and Actual Current Samples

D is defined here as the difference between the predicted and the actual current samples. In each sampling window, the last 25% of the samples in the window are predicted using the previous 75% of the samples in the sampling window based on linear prediction. Assume that the sampling frequency is 16 samples per cycle as shown in Fig. 2. To predict future values of a time series, linear prediction can be used.

$$I(m) \approx a_1 I(m-1) + a_2 I(m-2) + a_3 I(m-3) + \dots \quad (10)$$

In Eq. (10), $I(m)$ is the predicted m th value of I , and $I(m-1)$, $I(m-2)$ and ... are the past values of I . Since the

past I values are known, a_i coefficients can be found by using the LS approach.

For example, if we seek a third-order linear predictor, coefficient matrix $a = [a_1, a_2, a_3]^T$ is one of the solving of an overdetermined system of equations. If $I(m)$ is known for $1 \leq m \leq M-1$, then the overdetermined system of equations is given by Eq. (11).

$$\begin{bmatrix} I(4) \\ I(5) \\ \vdots \\ I(M-1) \end{bmatrix} \approx \begin{bmatrix} I(3) & I(2) & I(1) \\ I(4) & I(3) & I(2) \\ \vdots & \vdots & \vdots \\ I(M-2) & I(M-3) & I(M-4) \end{bmatrix} \begin{bmatrix} a_1 \\ a_2 \\ a_3 \end{bmatrix} \quad (11)$$

Eq. 11 can be written as $\bar{I} = Ha$ where H is a matrix of size $(M-4) \times 3$. Using the LS approach, the solution is given by $a = (H^T H)^{-1} H^T \bar{I}$; once the coefficients a_i are found, then $I(m)$ for $m \geq M$ can be estimated using Eq. (10).

As a result of a fault, the change in the current causes the predicted samples of the current waveform to deviate from their actual values as shown in Fig. 2. Since the window includes both pre- and during-fault data, the difference between the actual samples and the predicted samples is large. For the 16 samples per cycle, the last 4 samples are predicted. Therefore, parameter D , the difference between the predicted sample values and the actual sample values is defined as Eq. (12) shows.

$$D = \left| \frac{(S_{a13} + S_{a14} + S_{a15} + S_{a16}) \text{Actual values} - (S_{a13} + S_{a14} + S_{a15} + S_{a16}) \text{Predicted values}}{(S_{a13} + S_{a14} + S_{a15} + S_{a16})} \right| \quad (12)$$

C. Protection Scheme

In this section, the proposed protection scheme is explained stepwise. First, in each sampling window, the voltage PAS and the D value of the current for three phases are obtained. Second, the maximum values of PAS and D among three phases are calculated; the maximum values of D and PAS are named as D_{Max} and PAS_{Max} , respectively; calculation of the maximum value among three phases is to account for cases of unbalanced systems and asymmetrical faults. If the operating point $(x(D_{Max}, PAS_{Max}))$ of the relay is outside of the relay's normal operating area, the trip signal will be issued.

Since (D, PAS) measured under fault conditions behaves differently from the (D, PAS) measured for switching events at least in one dimension, it is possible to differentiate between a fault and switching events by using both D and PAS parameters and employing Mahalanobis Distance (MD) metric. MD is an effective tool to find outliers in multivariate data. The MD is unitless and scale-invariant. It also takes into account the correlations of the data. Another characteristic of MD is that it has an approximate chi-square distribution for normal multivariate observations. The Chi-Squared distribution is commonly used in applied statistics to provide the basis for making inferences about the variance of an arbitrary population based on a sample set of data [26]. Therefore, by determining the confidence ellipse of relay characteristic based upon the 99.9% quantile of the Chi-Square distribution with 2 degrees of freedom, it is possible to differentiate between the normal events and fault conditions.

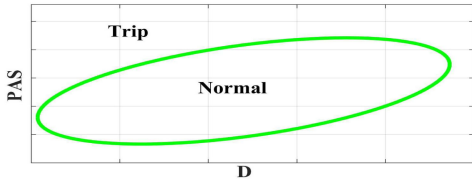


Fig. 3. Relay's characteristic; normal and trip area.

To explain the procedure of drawing the relay characteristic, consider matrix E that is formed based on the D and PAS measurement for normal events in the system such as load switching, transformer switching, and DG switching.

$$E = \begin{bmatrix} D_1 & D_2 & \dots & D_q \\ PAS_1 & PAS_2 & \dots & PAS_q \end{bmatrix} \quad (13)$$

where q is the total number of normal events, and each column contains the PAS and D measured for each event. MD of point $X = [D \text{ } PAS]^T$ is defined by Eq. (14):

$$MD^2(x|\mu, C) = (x - \mu)^T C^{-1} (x - \mu) \in R^1 \quad (14)$$

where μ is the sample mean vector defined by Eq. (15)

$$\mu = \left[\frac{1}{q} \sum_{i=1}^q D_i \text{ } \frac{1}{q} \sum_{i=1}^q PAS_i \right]^T \in R^{2 \times 1} \quad (15)$$

and C is the sample covariance matrix that is calculated by Eq. (16).

$$C = \frac{1}{q-1} \sum_{i=1}^q \left(\begin{bmatrix} D_i \\ PAS_i \end{bmatrix} - \mu \right) \left(\begin{bmatrix} D_i \\ PAS_i \end{bmatrix} - \mu \right)^T \in R^{2 \times 2} \quad (16)$$

As mentioned, the confidence ellipse of the relay characteristic is defined based upon the 99.9% quantile of the Chi-Square distribution with 2 degrees of freedom. The eigenvectors of the sample covariance matrix define the principal axes of the confidence ellipse, and the D and PAS mean values define the center of the ellipse. Also, the lengths of the major and minor axes of the ellipse, l_j , can be determined from the eigenvalues, λ_j , of the sample covariance matrix as Eq. (17) shows.

$$l_j = \sqrt{\lambda_j \chi_{2,99.9}^2} = \sqrt{13.816 \lambda_j} \quad (17)$$

Therefore, to determine the relay confidence ellipse, the following steps should be taken. First: switching scenarios are simulated, and corresponding PAS and D values for each relay are obtained. Second: matrix E is formed for each relay and the mean and covariance matrix is formed. Third: The confidence ellipse for each relay is determined by calculating the eigenvalues of the sample covariance matrix shown in Eq. (16). After the confidence ellipse is obtained, it can be stored in the relay. Fig. 3 shows the relay's characteristic; inside the confidence ellipse is the normal operating area whereas the outside is the trip area.

III. SIMULATION RESULTS AND DISCUSSION

In this section, the performance of the proposed protection scheme is evaluated through simulation of different scenarios in

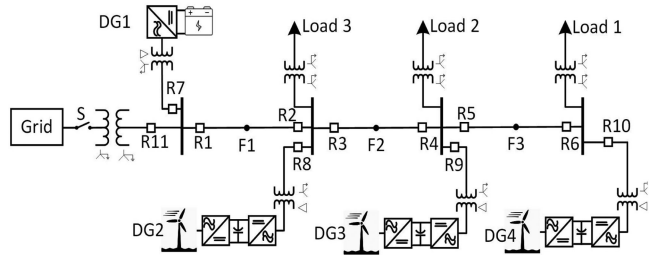


Fig. 4. System under study.

TABLE I
MICROGRID UNDER STUDY PARAMETERS

Main grid	500 MVA; 120kV	DG1	300kW
Grid transformer	24 MVA; 120/25kV; $X_t=0.04 \text{ pu}$	DG2, DG3, DG4	250kW
DG and load transformers	500 kVA; 0.6/25kV; $X_t=0.05 \text{ pu}$	Load 1	150kW
Lines impedance	$0.12+0.38j \text{ ohm/km}$	Load 2	350kW
Length of lines	250 m	Load 3	300kW

the system under study by using MATLAB Simulink software. The system under study is the modified CIGRE benchmark system [27], which includes a Battery Energy Storage (BES) and three type 4 wind turbines as shown in Fig. 4. The system parameters are shown in Table I. The inverters control systems in the system under study are the conventional dq control strategy for voltage source converters [28], [29]. The system is solidly grounded; the grid and load transformers configuration are Yg/Yg , and the DG transformers configuration are Δ/Yg . Fig. 4 also shows the relays installed at different points in the system. Each line is protected by two relays; line relays are directional. Also, a relay is allocated for the Point of Common Coupling (PCC) (R11) and each DG (R7 to R10). Each relay samples the local voltage and current. In the system under study, the Master-slave control strategy is employed. Information on the Master-slave control strategy can be found in [28]. In the system shown in Fig. 4, DG 1 is the Master controller working in Voltage-Frequency (VF) mode, and DG2 to DG4 are the slaves working in PQ mode. In PQ control mode, inverters transfer a determined active (P^0) and reactive power (Q^0) to the microgrid, and they do not considerably contribute to controlling the voltage and frequency parameters of the microgrid. Therefore, inverters with PQ control mode can only operate in the island mode when an inverter with VF control mode or a synchronous generator presents in the microgrid [29], [30]. In VF control mode, inverters control the amplitude and frequency of the output voltage like synchronous generators. [29], [30]. Table II demonstrates the investigated scenarios for the island and grid-connected modes. Through cases 1 and 2, the fault and switching scenarios for the island and grid-connected modes are inspected. The investigated fault scenarios include the Phase to Ground (PG), Phase to Phase (PP), Phase to Phase to Ground (PPG), Three Phase (3P) faults at points F1, F2, F3 in the island and grid-connected modes; in the island mode, the fault scenarios are performed for Bolted Faults (BF), Impedance Faults with $R_f = 4 \text{ ohms}$ (IF), and impedance faults with $R_f = 40 \text{ ohms}$; in the grid-connected mode, the fault scenarios are performed for BF, IF, and impedance faults with $R_f = 40 \text{ ohms}$.

TABLE II
INVESTIGATED SCENARIOS FOR THE ISLAND AND GRID-CONNECTED MODES

BF	Grid-connected Mode					
	Island Mode		Switching	IF ($R_f = 30$ ohms)	IF ($R_f = 20$ ohms)	
	IF ($R_f = 4$ ohms)	IF ($R_f = 40$ ohms)				
PG (F1, F2, F3)	x	x	x		x	x
PP (F1, F2, F3)	x	x	x		x	x
PPG (F1, F2, F3)	x	x	x		x	x
3P (F1, F2, F3)	x	x	x		x	x
Load 2			x	x		
Load 1=500kW			x			
Load 1=200kW+300kVar			x			
Load 1= 5MVA				x		
500kVA Transformer			x	x		
DG 3 Switching			x	x		

mode, the fault scenarios are performed for IF with $R_f = 40$, 30 and 20 ohms. To show the ability of the proposed scheme in distinguishing the normal events from the fault conditions, several load, transformer, and DG switching scenarios are also investigated as shown in Table II. The objective of examining the mentioned scenarios is to show that by using the two proposed parameters (PAS and D) and by employing the proposed protection scheme, all types of faults can be detected in the microgrid in both modes of operation; in case 3, the effect of the Short Circuit Capacity (SCC) of the grid feeder on the performance of the proposed protection scheme in the grid-connected mode is evaluated. The procedure of selecting switching scenarios to obtain relay characteristic is explained in case 4. In case 5, the effect of the inertia time constant on the performance of the proposed scheme is investigated. The impact of the presence of noise on the performance of the proposed scheme is evaluated in case 6. In case 7, the fault detection time of the proposed protection scheme is discussed; also, the proposed scheme is compared to the overcurrent and under-voltage fault detection methods in case 8. In case 9, the performance of the proposed method in a droop-controlled system is examined. Performance of the proposed scheme in the presence of synchronous generator in the microgrid is evaluated in case 10, and finally, the sensitivity of the confidence ellipse to changes in the microgrid arrangement is investigated in case 11.

A. Case 1: Island Mode – Fault and Switching Scenarios

In case 1, the fault and switching scenarios shown in Table II are investigated for the island mode. Different faults are applied at points F1, F2, and F3; PAS and D parameters are measured by the relays shown in Fig. 4.

In Fig. 5(a), PAS measured for the faults at points F1, F2, and F3 along with PAS measured for the DG, transformer, and load switching events in the island mode are shown and compared. The red surface in Fig. 5(a) shows the PAS measured by different relays for bolted PG, PP, PPG, and 3P faults; the light blue surface in Fig. 5(a) shows the PAS measured by different relays for PG, PP, PPG, and 3P faults with 4 ohms fault impedance ($R_f = 4$ ohms); also, the yellow surface in Fig. 5(a) shows the PAS measured by different relays for PG, PP, PPG, and 3P faults with 40 ohms fault impedance ($R_f = 40$ ohms); the orange surface

in Fig. 5(a) shows the PAS measured by different relays for the DG switching. Also, the PAS measured by different relays for transformer and load switching scenarios are shown by the dark blue surface. Fig. 5(a) contains three 3D space coordinate planes; each coordinate plane belongs to one fault location.

As demonstrated in Fig. 5(a), the maximum PAS for the switching events is 2.3 degrees (transformer switching); PAS for the phase to phase fault with $R_f = 40$ ohms is 8.24 degrees. As shown in Fig. 5(a), although the minimum PAS among the fault scenarios is for the phase to phase fault with $R_f = 40$ ohms, there is still a good margin between PAS for the phase to phase fault with $R_f = 40$ ohms and PAS for the switching events. This demonstrates that the voltage PAS can be employed for fault detection in the islanded microgrid.

The D parameter measured for the switching events is compared with the D parameter measured for different fault scenarios in Fig. 5(b). As explained in Section II-B the D parameter is obtained by analyzing the current waveform; for some relays in the system, the measured D value for the switching events and the fault scenarios are equal as shown in Fig. 5(b). It is because inverters are not able to provide more than 1.2 to 2 p.u current even in fault conditions. Therefore, current variation cannot be used separately in an inverter-based system to detect the fault, but it can be used as an indication of the fault conditions. As Fig. 5 demonstrates, by using the two proposed parameters together, it is possible to differentiate between switching events and fault conditions and detect the fault in the island mode of microgrid operation.

B. Case 2: Grid-Connected Mode- Fault and Switching Scenarios

In the grid-connected mode, the microgrid is connected to a 120 kV main grid bus bar with 500 MVA short circuit capacity. The fault and switching scenarios shown in Table II are investigated for the grid-connected mode in case 2. As shown for the island mode of operation, the impedance faults have the lower voltage PAS among fault scenarios; therefore, only the impedance faults are simulated for the grid-connected mode. In case 2, the impedance faults with $R_f = 40$, 30, and 20 ohms are applied at points F1, F2, and F3, and the PAS and D parameters are measured by the relays shown in Fig. 4.

PAS measured by the relays for the fault at points F1, F2, and F3, and PAS measured for the switching events are compared through Fig. 6(a) for the grid-connected mode. In Fig. 6(a), the green surfaces show the PAS measured by different relays for the PG, PP, PPG, and 3P faults with 40, 30, and 20 ohms fault impedance ($R_f = 40$, 30, and 20 ohms); The lighter the green color the lower the fault impedance. The orange surface in Fig. 6(a) shows the PAS measured by different relays for the DG switching scenarios. Also, the PAS measured by different relays for transformer and load switching scenarios are shown by the dark blue surface.

As it is shown in Fig. 6(a), the PAS is 1.5 degrees for the three-phase impedance fault with $R_f = 40$ ohms and 1.37 degrees for the phase to phase fault with $R_f = 40$ ohms; Fig. 6(a) also shows that the PAS increases as the fault impedance decreases;

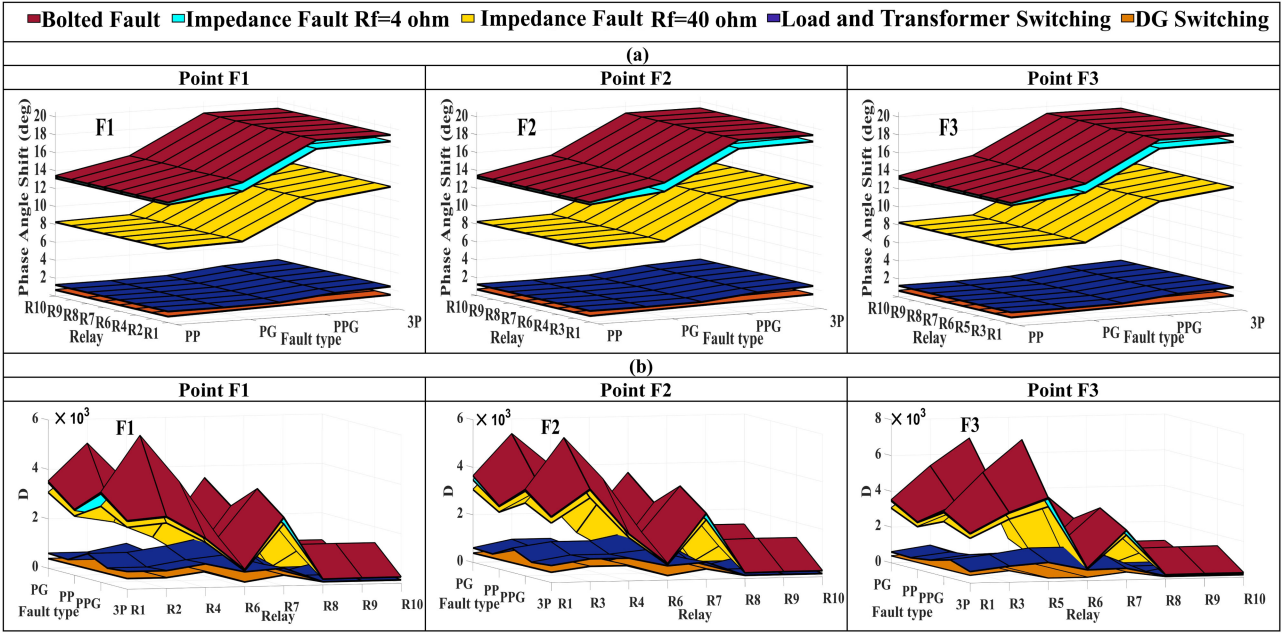


Fig. 5. (a) Maximum voltage PAS parameter and (b) D parameter measured by relays for the scenarios shown in Table II - Island mode. (a) Phase Angle Shift (PAS). (b) D Parameter.

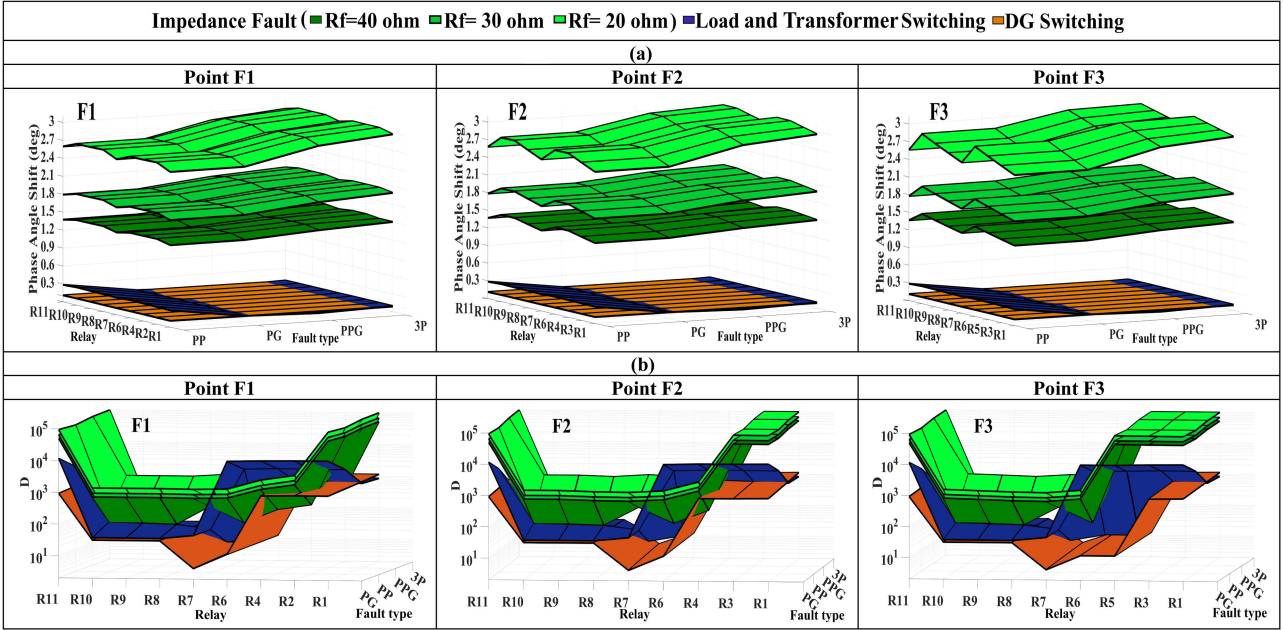


Fig. 6. (a) Maximum voltage PAS parameter and (b) D parameter measured by relays for the scenarios shown in Table II – Grid-connected mode of operation. (a) Phase Angle Shift (PAS). (b) D Parameter.

the maximum PAS for the switching events is 0.29 degrees ($P = 5$ MW switching) in the grid-connected mode. Also, the PAS for the DG switching is 0.11 degrees. Therefore, the PAS for the impedance fault ($R_f = 40$ ohms) is about 5 times of the PAS for the switching events, which shows fault conditions and switching events can be differentiated in the grid-connected mode by using the PAS parameter. As expected, the PAS is smaller in the

grid-connected mode compared to the island mode; therefore, different relay characteristics should be determined for the fault detection for each mode of operation.

The D value measured by the relays for the switching events and different fault scenarios are compared in Fig. 6(b). For the grid side relays (relays R1, R3, R5) there is a large margin between the measured D value for the switching events and the

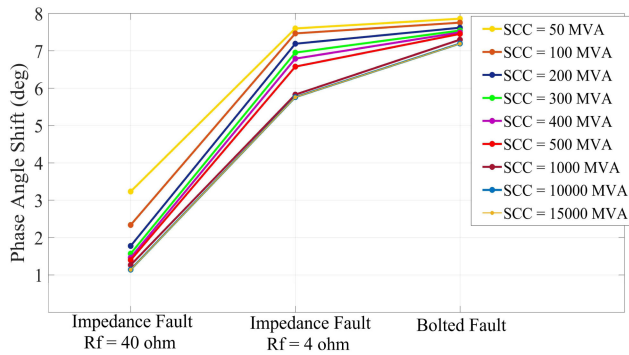


Fig. 7. PAS variations with variation of feeder SCC-Phase to ground fault (F2).

fault scenarios in the grid-connected mode. It is because, in the grid-connected mode, the microgrid is connected to the power system that is able to provide a high magnitude fault current. But, for the microgrid side relays (relays R2, R4, R6) the fault current and the switching current are close; for some relays, the fault and switching currents are almost the same; as mentioned before, it is because these relays (relays R2, R4, R6) only see the current coming from the IBRs and IBRs cannot provide more than 1.2 to 2 p.u current. Although the D parameter cannot be used separately to detect the fault in the grid-connected mode, the variation of the D parameter can be used as an indication of the fault in the system.

As shown in Fig. 5 and Fig. 6, by taking into account both parameters introduced above, fault can be detected in an inverter-based system in both island and grid-connected modes.

C. Case 3: The Effect of the Variation of the Short Circuit Capacity of the Grid Feeder on the Proposed Scheme

In this section, the effect of the SCC variations on the voltage PAS is examined. Fig. 7 demonstrates the PAS variation for impedance ($R_f = 4$ ohms and $R_f = 40$ ohms) and bolted phase to ground faults when feeder SCC changes. As Fig. 7 shows, although the phase angle shift decreases as the SCC of the grid feeder increases, there is a minimum voltage phase angle shift following a fault. In fact, there is a point that even if the short circuit capacity of the feeder increases, the voltage phase angle shift following a fault remains constant. For example, as Fig. 7 shows, the voltage PAS following a fault remains constant as SCC increases from 10000 MVA to 15000 MVA. This confirms the capability of the proposed protection scheme to detect the faults in the grid-connected mode regardless of the SCC power of the grid feeder.

D. Case 4: The Procedure of Selecting Switching Scenarios to Obtain Relay Characteristic

In selecting the switching scenarios to form the E matrix and obtain relay characteristic, the importance should be given to the different types of switching scenarios (such as DG, Transformer, and load switching) rather than the number of the performed scenarios. In general, the larger the sample size (the number of

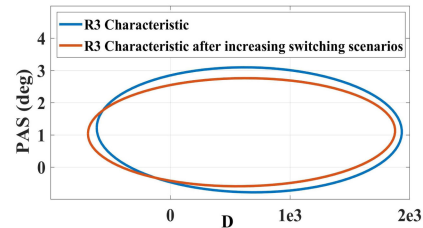


Fig. 8. Relay's R3 characteristic.

TABLE III
ADDED SWITCHING SCENARIOS

L= 200kW	L= 400kW
L= 300kW	L= 450kW
L= 100kW+150kVar	L= 150kW+200kVar

switching scenarios) the smaller the confidence ellipse [31]. For example, Fig. 8 compares the relay R3 characteristic for case 1 when the number of performed scenarios increases from 5 (shown in Table II) to 11. The added scenarios are shown in Table III. As Fig. 8 shows, the area of the confidence ellipse decreases as the number of the performed scenarios increases. Although by increasing the total number of the switching scenarios it is possible to determine the switching area with more precision, there is no need to perform a large number of switching scenarios to obtain the relay characteristics because of two main reasons: (a) there is a large margin between the PAS measured for switching events and fault condition as shown in case 1 and case 2; (b) the purpose here is to differentiate between switching events and fault conditions. Therefore, by considering the following switching scenarios to obtain relay characteristics, the required precision in determining relay characteristics for fault detection can be achieved.

- DG switching scenarios: connection and disconnection
- Transformer switching
- Load switching (largest load in the system)
- Load switching (active load with the maximum possible active power)
- Load switching (reactive load with the maximum possible reactive power)

E. Case 5: The Effect of the Inertia Time Constant on the Performance of the Proposed Scheme

Because of the presence of the power electronic interfaces, IBMs have a low inertia time constant [32], [33]. Therefore, the system frequency is susceptible to change during load switching, which may result in PAS variations. However, the power variations during a fault are larger than power variations during a switching event. Besides, frequency variations do not always result in PAS variations. It is because to obtain PAS, the phase angle of the two sampling windows that only have 0.00165 ($\alpha = 0.1K$) seconds time difference are compared. In fact, the frequency variations in the system should be very fast to result in PAS variations. In addition, PAS is associated with three main factors including (a) reactive power variation and its effect on the voltage level (b) active power interruption or variation and

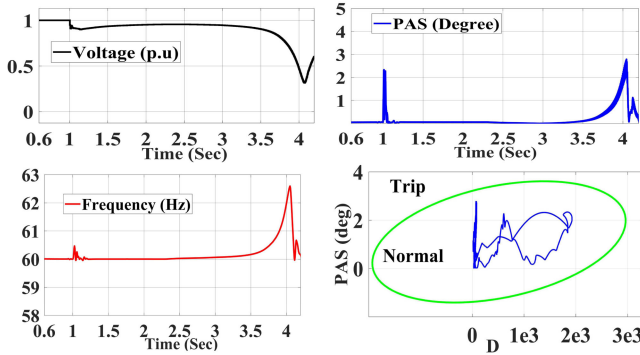


Fig. 9. Voltage, frequency, PAS, and relay R5 characteristic.

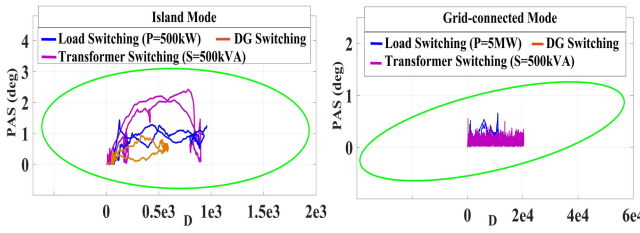


Fig. 10. R3 characteristic and (D, PAS) trajectory for the switching scenarios with the presence of the noise in the island and grid-connected modes.

its effect on frequency, and (c) changes in the grid equivalent impedance (X/R ratio). During a fault, all these three factors severely change as compared to a switching event; therefore a fault results in a larger PAS variation as compared to a switching event.

To demonstrate that PAS under fault is not comparable to PAS under load switching, an unlikely load-switching scenario is investigated. Load1 = 622 kVA ($P = 500 \text{ kW}$; $Q = 370 \text{ kVar}$) is connected to the islanded microgrid at $t = 1 \text{ sec}$ in one-step when the microgrid already has $S = 640 \text{ kVA}$ loading. The total generation power of the microgrid is 1050 kVA. By connecting this load, the total loading of the microgrid is 1262 kVA. Fig. 9 shows the voltage and frequency of the microgrid along with PAS measured by relay R5. The relay R5 characteristic and the (D, PAS) trajectory after the switching event are also shown in Fig. 9. As shown in Fig. 9, because of the excessive overload, the system is not stable. However, even for this aggressive switching scenario, the (D, PAS) trajectory is inside the confidence ellipse.

F. Case 6: The Impact of the Presence of the Noise on the Performance of the Proposed Scheme

In this section, the impact of the noise level on the sensitivity of the proposed method is evaluated by contaminating the voltage and current signals with white noise ($\text{SNR} = 25 \text{ dB}$). The relay R3 characteristic and the measured (D, PAS) trajectory for the switching scenarios with the presence of noise in the island and grid-connected modes are shown in Fig. 10. As can be seen in Fig. 10, all (D, PAS) trajectories are inside the normal operation area of the relay; therefore, the proposed scheme is able to properly operate in case of noisy measurements.

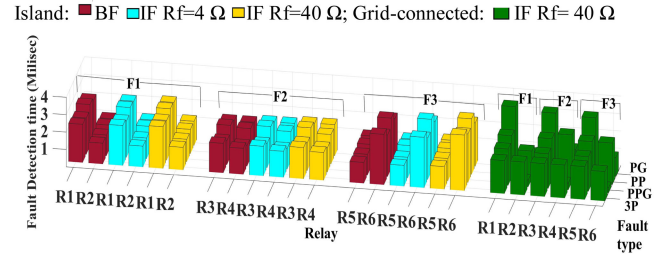


Fig. 11. Fault detection time of the relays for the investigated fault scenarios in the island and grid-connected modes.

TABLE IV
COMPARISON OF THE FAULT DETECTION TIME FOR BOLTED THREE-PHASE FAULT

Fault	Primary Relays	Fault Detection time (Sec)	
		Island	Grid-connected
F1	R1	10.15	0.0022
	R2	0.35	0.0012
F2	R3	2.3	0.0015
	R4	0.55	0.0015
F3	R5	0.19	0.0029
	R6	5.94	0.0029

G. Case 7: The Fault Detection Time of the Proposed Protection Scheme for the System Under Study

The fault detection time of the relays in the system under study for different fault scenarios at points F1, F2, and F3 in the island mode are shown in Fig. 11. The fault detection time of the relays for the impedance fault with $R_f = 40 \Omega$ at points F1, F2, and F3 in the grid-connected mode are also shown in Fig. 11(green bars). As can be seen in Fig. 11, all fault types on the feeder are detected by the primary relays in less than 5 milliseconds. Fig. 11 shows that the proposed protection scheme is able to effectively detect all types of fault in both microgrid operation modes. In fact, the current prediction enables the proposed method to recognize current variations fast; also, the method can distinguish between the normal events and the fault condition by measuring the PAS parameter, which leads to fast detection of the fault conditions in the system. It should be mentioned that the coordination between the relays can be achieved by employing a low-cost logic communication link between the relay at each end of the protection zone. When both relays at each end of the protected zone detect the front fault, the faulty zone will be removed from the system.

H. Case 8: Comparison of the Proposed Protection Scheme With Communication-assisted Overcurrent Protection, and Under Voltage Protection

At first, the proposed method is compared with a communication-assisted dual setting overcurrent protection presented in [34]. The comparison is made for bolted three-phase faults. Table IV compares the fault detection times of both methods for the fault at points F1, F2, and F3. As Table IV shows, for the proposed method, the primary relays detect the bolted three-phase fault at point F1 in 0.0022 and 0.0012 seconds in the

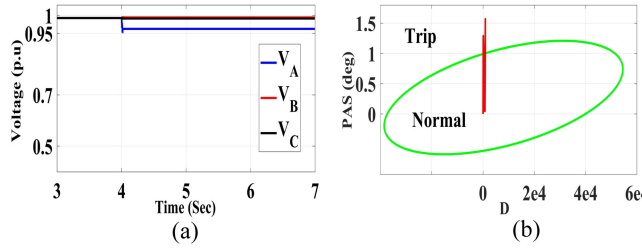


Fig. 12. (a) The voltage magnitudes measured by relay R6 and (b) relay R6 characteristic and (D, PAS) trajectory for impedance PG fault ($R_f = 40$ ohms) at point F3.

island mode; for communication assisted overcurrent protection [34], the primary relays detect the fault at point F1 in 10.15 and 0.35 seconds in the island mode. This shows that overcurrent-based protection methods are ineffective in IBMs. As mentioned earlier, depending on the inverter control design, the inverter may become disconnected from the system in the first 3 to 7 AC cycles after fault [9]; therefore, protection methods that have a fault detection time greater than 3 cycles can be considered ineffective for IBMs. Also, as the fault impedance increases the fault detection time of the overcurrent-based protection methods increase, and in most cases, the overcurrent protection cannot detect the impedance fault. But, as shown in Fig. 11 the proposed method detects all fault types in less than 1 AC cycle. Fig. 12(a) shows the voltage magnitudes measured by relay R6 when an impedance PG fault ($R_f = 40$ ohm) is applied to the system under study in the grid-connected mode at $t = 4$ sec at point F3. As shown in Fig. 12(a), all voltages are above 0.95 per unit and under-voltage protection cannot detect the fault. Relay R6 characteristic and (D, PAS) trajectory of the fault is demonstrated in Fig. 12(b). Both R5 and R6 detect this fault in less than 5 milliseconds as Fig. 11 shows.

I. Case 9: Performance of the Proposed Method in a Droop-Controlled System

In this section, the performance of the proposed protection scheme is examined when the droop-control strategy is employed in the system under study. In the droop control strategy, the output active and reactive power of the inverter depend on the frequency and magnitude of the output voltage, and they are regulated based on a droop characteristic [29]. In this case, DG1 and DG4 are working in droop-control mode, and DG2 and DG3 are working in PQ mode. The load switching scenarios shown in Table II are performed to obtain the relay characteristics based on the procedure explained in Section II-C. Relays R5 and R6 characteristics and (D, PAS) trajectory for the impedance PP fault with $R_f = 40$ ohms in the island mode are demonstrated in Fig. 13. Table V shows the relay fault detection time for the impedance 3P, PG, PP, and PPG faults with $R_f = 40$ ohms at points F1, F2, and F3 in the island mode for case 9. As Table V shows, the fault detection time of all relays are less than 16 milliseconds for impedance faults with $R_f = 40$ ohms at point F1, F2, and F3 in the island mode of operation. Therefore, this case study confirms the high performance of the proposed

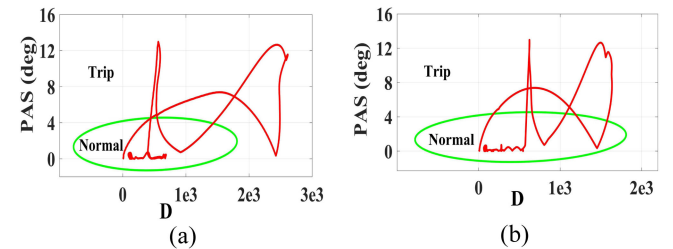


Fig. 13. (a) Relay R5 characteristic and (b) relay R6 characteristic, and (D, PAS) trajectories for the impedance PP fault ($R_f = 40$ ohms) at point F3 (Case 9).

TABLE V
RELAYS' FAULT DETECTION TIME (SEC) FOR CASE 9 AND CASE 10
(ISLANDED MODE)

	Case 9 (Droop-control)				Case 10 (in the presence of SG)			
	IF ($R_f = 40$ ohm)				IF ($R_f = 40$ ohm)			
	3P	PG	PP	PPG	3P	PG	PP	PPG
F1	R1 .0052	.0077	.0051	.0052	.0064	.0090	.0055	.0062
	R2 .0053	.0055	.0052	.0053	.0078	.0084	.0055	.0045
F2	R3 .0051	.0066	.0050	.0050	.0060	.0081	.0055	.0050
	R4 .0051	.0063	.0050	.0051	.0104	.0097	.0054	.0057
F3	R5 .0050	.0051	.0049	.0050	.0053	.0068	.0053	.0042
	R6 .0049	.0050	.0049	.0049	.0104	.0107	.0053	.0065

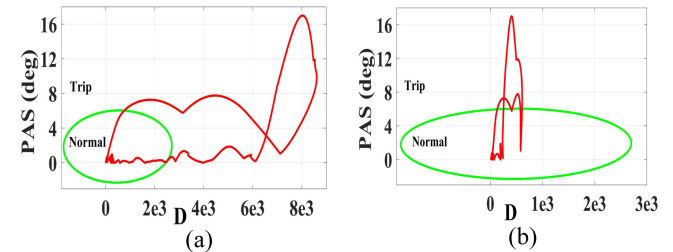


Fig. 14. (a) Relay R5 characteristic and (b) relay R6 characteristic, and (D, PAS) trajectories for the impedance PP fault ($R_f = 40$ ohms) at point F3 (case 10).

protection scheme when the droop control strategy is employed in the system.

J. Case 10: Performance of the Proposed Method in the Presence of Synchronous Generator in the Microgrid

To examine the performance of the proposed method in the presence of a synchronous generator in the microgrid, BES (DG1) is replaced with a 0.5 MVA synchronous generator. In this case, the synchronous generator forms the voltage and frequency of the microgrid in the island mode and DG2 to DG 4 are working in PQ mode. The load switching scenarios depicted in Table II are performed to obtain the relay characteristics based on the procedure explained in Section II-C.

Relays R5 and R6 characteristics and (D, PAS) trajectory for the impedance PP fault with $R_f = 40$ ohms in the island mode are shown in Fig. 14. Table V demonstrates the relay fault detection time for impedance 3P, PG, PP, and PPG faults with $R_f = 40$ ohms at points F1, F2, and F3 in the island mode for case 10. As Table V depicts, the fault detection time of all relays are less than 16 milliseconds for impedance faults with $R_f = 40$ ohms

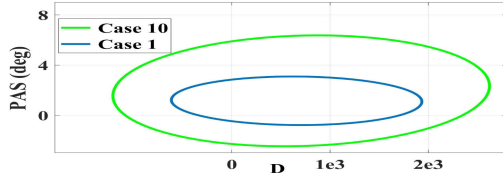


Fig. 15. Relay's R3 characteristic.

at point F1, F2, and F3 in the island mode of operation, which verifies the performance of the method in the presence of the synchronous generator in the microgrid.

K. Case 11: Sensitivity of the Confidence Ellipse to Changes in the Microgrid Arrangement

Regular microgrid arrangement changes such as DG switching, overload condition, the connection of a new load or transformer, and disconnection of a load are considered in the procedure of determining the relay characteristic. In fact, the confidence ellipse determines the area of the switching events, and as shown in case 5, even an aggressive switching event does not affect the performance of the method. Therefore, there is no need to recalculate the relay setting in case of these arrangement changes. However, it may be needed to recalculate the relay setting if the voltage-frequency control strategy of the microgrid changes (for example, when the battery is replaced with a synchronous generator). Fig. 15 compares relay R3 confidence ellipse for the first case study and case 10. As Fig. 15 shows, the confidence ellipse is larger in the presence of a synchronous generator in the system. Instead of recalculating the relay settings, it is also possible to set the relay characteristic based on the case scenario with the largest ellipse (worst-case scenario). In case of determining the relay characteristics based on the case scenario with the largest ellipse, there is no need to change the relays' setting if the control strategy changes; but, a protection study is needed to make sure that selecting the relay characteristics based on the worst-case scenario does not affect the fault detection procedure. Between the three control strategies investigated in case 1 (Master-Slave), case 9 (droop-control), and case 10 (synchronous generator), the relays characteristic obtained for case 10 have the largest obtained ellipses. To examine the performance of the proposed method when unique group settings is chosen for different control strategies, all relays' settings are chosen based on the settings obtained in case 10; then, the proposed method is reexamined with the new settings for case 1 and case 9. Table VI shows the relays fault detection time for the impedance 3P, PG, PP, and PPG faults with $R_f = 40$ ohms at points F1, F2, and F3 in the island mode for case 1 and case 9 when all the relay characteristics are set based on the settings obtained in case 10. As shown in Table VI, although the fault detection time of the relays slightly increases compared to Table V, all fault detection times are still less than 16 milliseconds when the relays' settings are chosen based on the settings obtained in case 10. Therefore, the system under study can be protected using a unique group of relays' setting in case 1, case 9, and case 10.

TABLE VI
RELAYS' FAULT DETECTION TIME (SEC) FOR CASE 1 AND CASE 9 (ISLANDED MODE) USING THE RELAY SETTING OBTAINED IN CASE 10

Case 1 (Master-slave)				Case 9 (Droop-control)					
		IF ($R_f=40$ ohm)				IF ($R_f=40$ ohm)			
		3P	PG	PP	PPG	3P	PG	PP	PPG
F1	R1	.0069	.0067	.0046	.0069	.0085	.0087	.0056	.0098
	R2	.0069	.0055	.0046	.0066	.0074	.0065	.0057	.0070
F2	R3	.0048	.0054	.0045	.0047	.0080	.0076	.0056	.0079
	R4	.0072	.0067	.0035	.0072	.0079	.0074	.0057	.0077
F3	R5	.0043	.0047	.0034	.0042	.0077	.0071	.0055	.0075
	R6	.0073	.0074	.0034	.0077	.0081	.0081	.0055	.0082

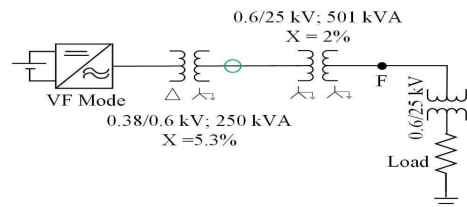


Fig. 16. Experimental setup.

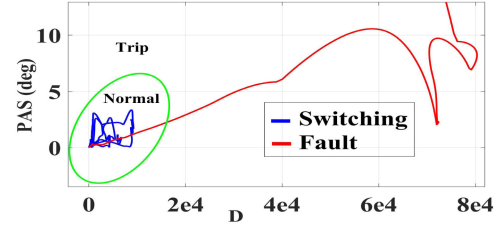


Fig. 17. Relay characteristic and (D, PAS) trajectory for the switching and fault scenarios.

IV. EXPERIMENT RESULTS

The experiment results are obtained on the Hydro-Québec's Research Institute (IREQ) 25 kV distribution test line. The system has two overhead lines which are approximately 100 m long. The test line includes a synchronous generator, motors, BES, and controllable RLC load; The BES is 100 kWh in total and it is connected to the system through an inverter. The experimental setup to examine the performance of the proposed protection scheme is shown in Fig. 16. The experimental setup includes the BES and load as shown in Fig. 16. The green cycle in Fig. 16 shows where the measurements are taken. Four scenarios are investigated which include the phase to ground fault, resistive load switching with $R = 100$ kW, $R = 50$ kW, and capacitive load switching with $C = 50$ kVar. The mentioned scenarios are performed in the island mode, and the inverter is working in VF control mode. The phase to ground fault is applied to the system at point F (shown in Fig. 16) when the inverter is working in full load condition. For the switching scenarios, the load is connected to the inverter when the inverter has no load. Fig. 17 shows the relay characteristic, (D, PAS) trajectory for switching scenarios (blue line), and (D, PAS) trajectory for fault scenario (red line). As Fig. 17 shows, the fault is detected in 4.22 milliseconds after fault; this is the time that (D, PAS) trajectory enters the trip area.

TABLE VII
PAS AND D FOR FAULT AND SWITCHING SCENARIOS

	PAS (Degrees)	D parameter
Phase to ground fault (PG) at point F	12.94	8.030e04
Load switching (R=100kW)	3.36	9.437e03
Load switching (R=50kW)	1.1	4.428e3
Load switching (C=50kVar)	2.68	6.575e03

The PAS and D values measured for each scenario are shown in Table VII. It is worth mentioning that the PAS measured for worst-case switching scenario R = 100kW (equal to the total BES power) is 3.36 degrees which still has a good margin with PAS = 12.94 degrees measured for the fault scenario.

The results confirm that the proposed protection scheme effectively detects the fault in the experimental test-bench.

V. CONCLUSION

A protection scheme was presented in this paper to detect feeder faults in IBM in both modes of operation. This scheme uses a new relay characteristic to detect the fault. The proposed method was tested in the modified CIGRE benchmark system using MATLAB Simulink software. It was demonstrated that the proposed scheme is able to detect a fault in less than 16 milliseconds; it can protect the IBM in both operating modes, the island and grid-connected modes. It was also shown that the proposed method can effectively protect the microgrid in the presence of a synchronous generator in the microgrid. Experimental tests were also performed in the IREQ distribution test line which confirms that the proposed protection scheme is able to detect a fault in less than 16 milliseconds.

REFERENCES

- [1] D. T. Ton and M. A. Smith, "The U.S. department of energy's microgrid initiative," *The Electricity J.*, vol. 25, no. 8, pp. 84–94, 2012.
- [2] N. Pogaku, M. Prodanovic, and T. C. Green, "Modeling, analysis and testing of autonomous operation of an inverter-based microgrid," *IEEE Trans. Power Electron.*, vol. 22, no. 2, pp. 613–625, Mar. 2007.
- [3] S. Chowdhury, S. P. Chowdhury, and P. Crossley, "Microgrids and active distribution networks," Stevenage: Inst. Eng. Technol., London, U.K., 2009.
- [4] A. Hooshyar and R. Iravani, "Microgrid protection," *Proc. IEEE*, vol. 105, no. 7, pp. 1332–1353, Jul. 2017.
- [5] S. S. Venkata, M. J. Reno, W. Bower, S. Manson, J. Reilly, and G. W. Sey, Jr., "Microgrid protection: Advancing the state of the art," SANDIA National Laboratories, SAND2019-3167, United States, Mar. 2019.
- [6] Z. Shuai, C. Shen, X. Yin, X. Liu, and Z. J. Shen, "Fault analysis of inverter-interfaced distributed generators with different control schemes," *IEEE Trans. Power Del.*, vol. 33, no. 3, pp. 1223–1235, Jun. 2018.
- [7] W. Guo, L. Mu, and X. Zhang, "Fault models of inverter-interfaced distributed generators within a low-voltage microgrid," *IEEE Trans. Power Del.*, vol. 32, no. 1, pp. 453–461, Feb. 2017.
- [8] *IEEE Standard for Interconnection and Interoperability of Distributed Energy Resources With Associated Electric Power Systems Interfaces*, IEEE Standard 1547-2018 (Revision of IEEE Standard 1547-2003), pp. 1–138, Apr. 2018.
- [9] J. Keller and B. Kroposki, "Understanding fault characteristics of inverter-based distributed energy resources," Nat. Renewable Energy Lab. (NREL), Golden, CO (United States), Tech. Rep. NREL/TP-550-46698, Jan. 2010.
- [10] S. F. Zarei, H. Mokhtari, and F. Blaabjerg, "Fault detection and protection strategy for islanded inverter-based microgrids," *IEEE J. Emerg. Sel. Topics Power Electron.*, vol. 9, no. 1, pp. 472–484, Feb. 2021.
- [11] Z. Liang, X. Lin, Y. Kang, B. Gao, and H. Lei, "Short circuit current characteristics analysis and improved current limiting strategy for three-phase three-leg inverter under asymmetric short circuit fault," *IEEE Trans. Power Electron.*, vol. 33, no. 8, pp. 7214–7228, Aug. 2018.
- [12] S. F. Zarei, H. Mokhtari, and F. Blaabjerg, "Fault detection and protection strategy for islanded inverter-based microgrids," *IEEE J. Emerg. Sel. Topics Power Electron.*, vol. 9, no. 1, pp. 472–484, Feb. 2021.
- [13] J. Q. Yu, Y. Hou, A. Y. S. Lam, and V. O. K. Li, "Intelligent fault detection scheme for microgrids with wavelet-based deep neural networks," *IEEE Trans Smart Grid*, vol. 10, no. 2, pp. 1694–1703, Mar. 2019.
- [14] M. Mishra and P. K. Rout, "Detection and classification of micro-grid faults based on HHT and machine learning techniques," *IET Gener. Transmiss. Distrib.*, vol. 12, no. 2, pp. 388–397, 2018.
- [15] F. Zhang and L. Mu, "A fault detection method of microgrids with grid-connected inverter interfaced distributed generators based on the PQ control strategy," *IEEE Trans. Smart Grid*, vol. 10, no. 5, pp. 4816–4826, Sep. 2019.
- [16] S. F. Zarei and M. Parniani, "A comprehensive digital protection scheme for low-voltage microgrids with inverter-based and conventional distributed generations," *IEEE Trans. Power Del.*, vol. 32, no. 1, pp. 441–452, Feb. 2017.
- [17] Z. Chen, X. Pei, M. Yang, L. Peng, and P. Shi, "A novel protection scheme for inverter-interfaced microgrid (IIM) operated in islanded mode," *IEEE Trans. Power Electron.*, vol. 33, no. 9, pp. 7684–7697, Sep. 2018.
- [18] H. Muda and P. Jena, "Superimposed adaptive sequence current based microgrid protection: A new technique," *IEEE Trans. Power Del.*, vol. 32, no. 2, pp. 757–767, Apr. 2017.
- [19] X. Liu, M. Shahidehpour, Z. Li, X. Liu, Y. Cao, and W. Tian, "Protection scheme for loop-based microgrids," *IEEE Trans Smart Grid*, vol. 8, no. 3, pp. 1340–1349, May 2017.
- [20] B. Bak-Jensen *et al.*, "Protection of distribution systems with distributed energy resources," CIGRE (International Council on Large Electric Systems), Paris, France, 2015.
- [21] S. Kar, S. R. Samantaray, and M. D. Zadeh, "Data-mining model based intelligent differential microgrid protection scheme," *IEEE Syst. J.*, vol. 11, no. 2, pp. 1161–1169, Jun. 2017.
- [22] S. Chen, N. Tai, C. Fan, C. Fan, J. Liu, and S. Hong, "Sequence-componentbased current differential protection for transmission lines connected with IIGs," *IET Gener. Transmiss. Distrib.*, vol. 12, no. 12, pp. 3086–3096, Oct. 2018.
- [23] M. H. J. Bollen, *Understanding Power Quality Problems: Voltage Sags and Interruptions*. Hoboken, NJ, USA: Wiley-IEEE Press, 2000.
- [24] S. Z. Djokic and J. V. Milanovic, "Advanced voltage sag characterisation. Part I: Phase shift," *IEE Proc. - Gener. Transmiss. Distrib.*, vol. 153, no. 4, pp. 423–430, Jul. 2006.
- [25] S. Z. Djokic, J. V. Milanovic, and S. M. Rowland, "Advanced voltage sag characterisation II: Point on wave," *IET Gener. Transm. Distrib.*, vol. 1, no. 1, pp. 146–154, Jan. 2007.
- [26] J. S. Milton and J. C. Arnold, *Introduction to Probability and Statistics: Principles and Applications for Engineering and the Computing Sciences* (Schaum's Solved Problems Series). 3rd ed. New York, NY, USA: McGraw-Hill, 1995.
- [27] K. Strunz, E. Abbasi, R. Fletcher, N. Hatziargyriou, R. Iravani, and G. Joos, "Benchmark systems for network integration of renewable and distributed energy resources," CIGRE (International Council on Large Electric Systems), Paris, France, 2014.
- [28] W. C. Shan, L. X. Lin, G. Li, and L. Y. Wei, "A seamless operation mode transition control strategy for a microgrid based on master-slave control," in *Proc. 31st Chin. Control Conf.*, 2012, pp. 6768–6775.
- [29] J. Rocabert, A. Luna, F. Blaabjerg, and P. Rodríguez, "Control of power converters in AC microgrids," *IEEE Trans. Power Electron.*, vol. 27, no. 11, pp. 4734–4749, Nov. 2012.
- [30] J. A. P. Lopes, C. L. Moreira, and A. G. Madureira, "Defining control strategies for microgrids islanded operation," *IEEE Trans. Power Syst.*, vol. 21, no. 2, pp. 916–924, 2006.
- [31] C. D. Ghilani and P. R. Wolf, *Adjustment Computations: Spatial Data Analysis*. 4th ed. Hoboken, NJ, USA: Wiley, 2006.
- [32] E. Dehghanpour, H. K. Karegar, and R. Kheirollahi, "Under frequency load shedding in inverter based microgrids by using droop characteristic," *IEEE Trans. Power Del.*, vol. 36, no. 2, pp. 1097–1106, Apr. 2021.
- [33] P. Mahat, Z. Chen, and B. Bak-Jensen, "Underfrequency load shedding for an islanded distribution system with distributed generators," *IEEE Trans. Power Del.*, vol. 25, no. 2, pp. 911–918, Apr. 2010.
- [34] H. M. Sharaf, H. H. Zeineldin, and E. El-Saadany, "Protection coordination for microgrids with grid-connected and islanded capabilities using communication assisted dual setting directional overcurrent relays," *IEEE Trans. Smart Grid*, vol. 9, no. 1, pp. 143–151, Jan. 2018.



Ehsan Dehghanpour (Student Member, IEEE) received the M.S. degree in electrical engineering from Shahid Beheshti University, Tehran, Iran, in 2016. He is currently working toward the Ph.D. degree with the Department of Electrical and Computer Engineering, McGill University, Montreal, QC, Canada. His main research interests include DC and AC microgrids, power systems protection, and optimization algorithms.



Géza Joós (Life Fellow, IEEE) received the M.Eng. and Ph.D. degrees in electrical engineering from McGill University, Montreal, QC, Canada, in 1974 and 1987, respectively. He was with ABB, École de Technologie Supérieure and Concordia University, Montreal, QC, Canada. Since 2001, he has been a Full Professor with McGill University and holds the NSERC/Hydro-Québec Industrial Research Chair on the Integration of Renewable Energies and Distributed Generation into the Electric Distribution Grid. He is involved in fundamental and applied research related to the application of high-power electronics to power conversion, including distributed generation and wind energy, to power system compensation, and to the integration of renewable energy and distributed generation into electric grids. Dr. Joós is active in a number of IEEE Industry Applications Society committees and in the IEEE Power Engineering Society and CIGRE working groups, including Study Committee C6 on Distribution Systems and Dispersed Generation. He is a Fellow of the Canadian Academy of Engineering and the Engineering Institute of Canada.



Michel Normandea (Member, IEEE) received the B.Sc. degree in electrical engineering from École de Technologie Supérieure, Montréal, QC, Canada, in 2003, and the M.Sc. degree in electrical engineering from École Polytechnique de Montréal, Montreal, QC, Canada, in 2017. In November 2009, he joined Hydro-Québec electricity supply. He leads the testing and validation of the distributed energy resources interconnection and integration approaches developed by McGill researchers in the Hydro-Québec research laboratory and test facilities. His main research interests include power system protection and inverter-based Microgrids stability and control.



Yves Brissette (Life Senior Member, IEEE) is a retired Senior Researcher with IREQ (Hydro Québec's Research Institute). He has mainly worked on High voltage circuit breakers, superconducting current limiters, and overheard ground wire power supply. He has also dedicated the past 15 years to the study of the distribution networks and apparatus and is the father of the IREQ's medium voltage distribution test line. He has supervised students at the master and Ph.D. level in the context of the Renewable Energy chair of McGill University. He is an Invited Professor with École Polytechnique of Montréal, where he teaches Materials and Network Apparatus for the past six years. He is a Member of Ordre des Ingénieurs du Québec.